CHEMISTRY OF MATERIALS

pubs.acs.org/cm

Article

Boosting Catalytic Lifetime in Chemical Vapor Deposition of Carbon Nanotubes by Rapid Thermal Pretreatment of Alumina-Supported Metal Nanocatalysts

Jaegeun Lee,[⊥] Golnaz Najaf Tomaraei,[⊥] Moataz Abdulhafez, and Mostafa Bedewy*

Cite This: *Chem. Mater.* 2021, 33, 6277−6289

Read Online

ACCESS | Metrics & More | Article Recommendations | Supporting Information

ABSTRACT: In this paper, we present an approach for boosting the catalytic lifetime in the growth of carbon nanotubes (CNTs) by chemical vapor deposition from an oxide-supported metal catalyst. We leverage a rapid thermal pretreatment to decouple the catalyst nanoparticle formation step, by solid-state dewetting, from the catalytic activation and CNT growth step. We find that the CNT yield significantly increased with the increasing catalyst formation temperature. To reveal the mechanism, we combined real-time kinetics measurements with a comprehensive characterization of the catalyst and support films after annealing in a reducing environment. Our results reveal that the observed threefold boost in CNT growth at higher catalyst formation temperatures results from an increased catalytic lifetime rather than an increased reaction rate. Atomic force microscopy analysis of the catalyst nanoparticles revealed that the loss of the catalyst by subsurface diffusion was suppressed, which delayed catalyst deactivation. The properties of the alumina film after annealing at different temperatures were analyzed by ellipsometry, nanoindentation, X-ray diffraction, and contact angle measurement. We show that annealing at 900 °C in hydrogen results in denser and less porous alumina than lower temperature annealing. Both film crystallinity and Lewis basicity also increased with a higher annealing temperature, highlighting the capability of our approach to tune the catalytic performance by tailoring the oxide support via a single thermochemical pretreatment step. Hence, this decoupled process can enable the growth of longer CNTs that is not achievable by conventional coupled recipes.

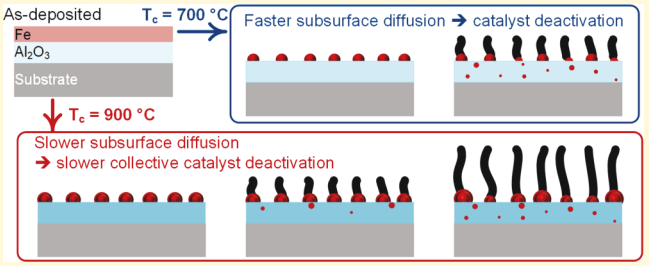

1. INTRODUCTION

An individual carbon nanotube (CNT) is an anisotropic nanostructure that has an extraordinarily high aspect ratio. The synthesis of longer CNTs has been persistently pursued,[1−5] and the highest aspect ratio ever reported reaches 10^8.[6] Importantly, many applications of CNT ensembles require long CNTs for better performance, such as the increased mechanical strength and electrical conductivity of yarns made from high aspect ratio individual CNTs.[7] Hence, for the successful commercialization of CNTs, the ability to mass-produce long and highly aligned CNTs is highly demanded.

A typical method for the high-yield synthesis of CNTs is catalytic chemical vapor deposition (CVD) using a supported metal catalyst.[2−5,8,9] This CVD growth process typically proceeds according to the following two steps: first, the formation of catalyst nanoparticles by thin-film dewetting and second, the nucleation and growth of CNTs from the seeding catalyst nanoparticles. The first step of catalyst formation determines the initial chemical state of metal nanoparticles, their number density, and size distribution.[10,11] Alumina is widely used as a support material because of its excellent performance in a wide range of experimental conditions.[8,9,12−14] Nevertheless, the synthesis of long CNTs is still challenging because of the limited lifetime of the catalyst.

Catalyst nanoparticles evolve both physically and chemically during the CNT growth step and eventually deactivate after a certain period of time, referred to as the catalytic lifetime, which depends on the growth conditions. Various mechanisms for catalytic deactivation were previously reported, including chemical poisoning,[15,16] carbon overcoating,[10,17] mechanical coupling,[18,19] and catalyst loss by migration on the surface as well as to the underlying layer.[20−22] These deactivation phenomena are dependent on both the initial state of the catalyst and support at the beginning of the growth step and the experimental conditions during the CNT growth step. Thus, the conditions of both the catalyst formation step and the CNT growth step influence the lifetime of a catalyst.

Received: December 8, 2020
Revised: July 7, 2021
Published: August 6, 2021

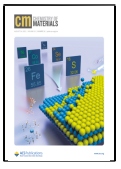

Table 1. Demonstration of the Unique Approach in This Study to Decouple Both Gas-Phase Reactions and Catalyst Formation from the Catalytic Growth of CNTs, Compared to Previous Reports on Decoupling Either Gas-Phase Reactions or Catalyst Formation from the Catalytic Growth of CNTs

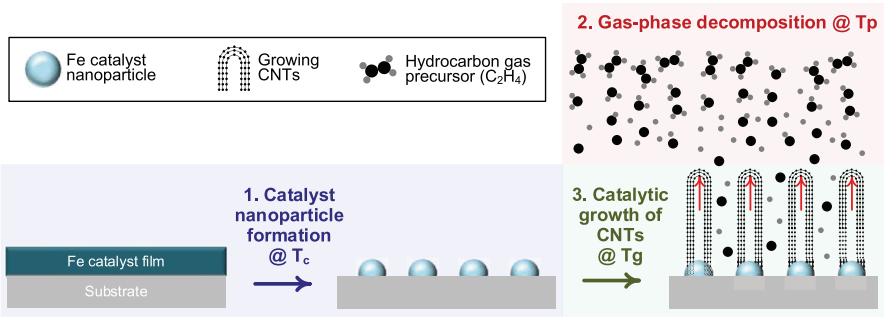

Schematic demonstrating the decoupling of the three different processes involved in CNT forest growth: (1) catalyst formation, (2) gas-phase reactions, and (3) catalytic growth of CNTs.

corresponding author/group leader	year	decoupling gas-phase reactions from CNT growth	decoupling catalyst formation from CNT growth	method/approach of decoupling	references
Cheol Jin Lee	2001	**decoupled**	coupled	preheater	24
Young Hee Lee	2002	**decoupled**	coupled	tungsten wire filament	25
Robert H. Hauge	2008	**decoupled**	coupled	hot filament	26
A. John Hart	2009	**decoupled**	coupled	preheater	27
Carl V. Thompson	2009	**decoupled**[a]	coupled	preheater	28
Guofang Zhong/John Robertson	2009	**decoupled**	coupled	plasma	29
Gilbert D. Nessim	2011	**decoupled**	coupled	preheater	30
Suguru Noda	2012	**decoupled**	coupled	preheater	31
Hyung Gyu Park	2013, 2018	**decoupled**[a]	coupled	temperature gradient within the reactor	32,33
Kenji Hata	2013	coupled	**decoupled**	fast heating by infrared	34,35
A John Hart	2016	coupled	**decoupled**[b]	moving the substrate	36
Mostafa Bedewy	2021	**decoupled**	**decoupled**	preheater and rapid heating by infrared	present work

[a]Temperature of the gas-phase reaction zone affects the temperature of the substrate, i.e., not perfectly decoupled. [b]The growth and catalyst formation were performed at the sample temperature, although the steps are decoupled.

One can suggest that these steps may be independently controlled by thermally treating alumina in a hydrogen-rich environment, for example, in a separate step prior to inserting into a CVD reactor. However, since iron is easily oxidized when exposed to an ambient atmosphere, this method is impractical as an approach for decoupling the catalyst formation step from the CNT growth step. Hence, a closed system is required, which can enable rapidly changing the conditions after the catalyst formation step (i.e., right before the growth step). A major problem is that in the conventional design of CVD growth recipes, the temperature for the catalyst formation step (T_c) is either the same as, or strongly coupled to, that of the CNT growth step (T_g). This is mainly because of the experimental difficulty in changing the reactor temperature instantaneously, especially for hot-walled reactors. Therefore, with the conventional coupled recipe, it is difficult to independently investigate the effect of T_g and T_c on the catalytic lifetime.

To maximize the catalytic lifetime, it is ideal to optimize the catalyst formation step and CNT growth step by independently controlling the conditions in each step. Recently, we demonstrated that complete decoupling of catalyst formation and CNT growth is possible by leveraging the capabilities of a custom-designed rapid thermal CVD reactor and showed that there is an inverse relationship between the density of CNTs and T_g, while there is no significant dependence of density on the T_c.[23] Our decoupling approach based on combining rapid thermal processing with a preheater in a multizone CVD reactor is a powerful tool that enables the investigation of previously unexplored combinations of process parameters for each of the two steps of catalyst formation and CNT growth. While there have been several efforts to achieve partial decoupling, as summarized in Table 1, these reports decoupled either only gas-phase reactions from CNT growth or only decoupled catalyst formation from CNT growth.[24−36] In fact, most of the previous studies decoupled gas-phase reactions, and there were only two groups that decoupled catalyst formation.[34,36] Using our decoupled recipe approach, we uniquely achieve independent control of T_c, T_g, and the gas precursor decomposition temperature in the preheater (T_p).

Here, we show that our unique approach of decoupling T_c and T_g enables a significant increase of the catalytic lifetime based on tuning the rapid thermal pretreatment step for an alumina-supported iron catalyst. When T_c is much higher than T_g, we observe a threefold boost in the catalytic lifetime. The analyses of the alumina layer before and after annealing at different T_c values showed that a denser and less porous phase is formed at higher T_c values, which delays subsurface diffusion of the catalyst into the alumina layer, delaying deactivation.

2. EXPERIMENTAL SECTION

2.1. CNT Forest Growth. CNTs were grown in a custom-designed multizone rapid thermal CVD reactor (CVD Equipment, Central Islip, NY) (Figure 1a). Detailed experimental information is described in our recent publication.[23] Briefly, a piece of catalyst-coated substrate [1 nm of Fe by e-beam evaporation on 10 nm of alumina by atomic layer deposition on a silicon (100) wafer with a 300 nm thick SiO_2 layer] was loaded into the reactor. Growth

https://doi.org/10.1021/acs.chemmater.0c04692
Chem. Mater. 2021, 33, 6277−6289

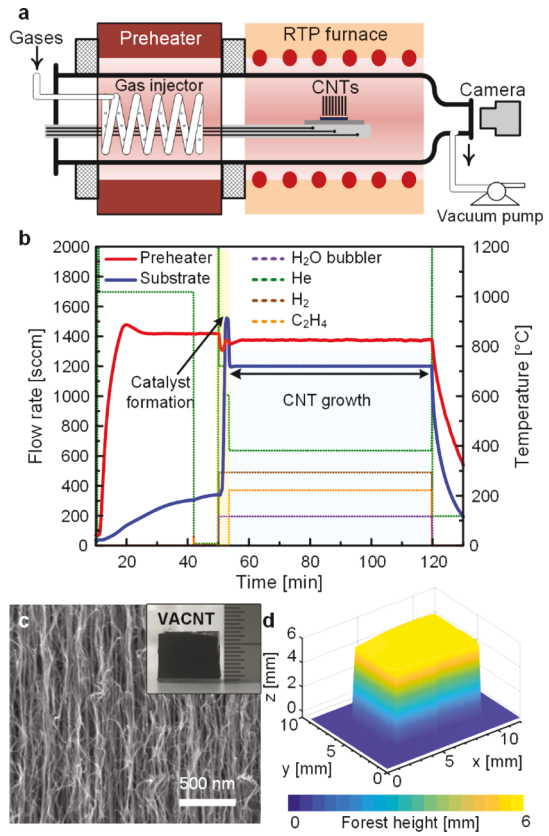

Figure 1. (a) Schematic representation of a RTP-CVD reactor. (b) Example of a decoupled recipe where $T_c > T_g$. (c) SEM image of a representative CNT forest with its photo as an inset. (d) Digital 3D data for the geometry of a CNT forest obtained by 3D optical microscopy.

experiments were run automatically according to a programmed recipe. A typical growth recipe is shown in Figure 1b, in which T_c and T_g are decoupled (here, $T_c > T_g$). During the catalyst formation step, the flow rates of H_2, He, and He through the water bubbler were 490, 1010, and 200 sccm, respectively. After that, the temperature was changed rapidly from T_c to T_g, and the time for this transition was kept constant at 20 s for all growth runs. During the growth step, the flow rates of C_2H_4, H_2, He, and He through the water bubble were 370, 490, 640, and 200 sccm, respectively. The preheater temperature was kept constant for all experiments at 825 °C. The morphology of the as-grown CNT forests was analyzed by scanning electron microscopy (SEM) using JEOL JSM-6510, which shows the successful growth of tall vertically aligned CNTs, referred to as CNT forests (Figure 1c). The number of walls and outer diameter of CNTs were observed by transmission electron microscopy (TEM) using Hitachi H9500. The structural quality was analyzed by Raman spectroscopy (Xplora, Horiba Scientific) using the 638 nm excitation wavelength.

2.2. Measuring Height and Growth Kinetics of the CNT Forest. The average height of the CNT forest was calculated by dividing the volume of the CNT forest by the area of the substrate on which the CNT forest was grown. For the accurate measurement of the volume of the CNT forest, a 3D optical microscope (VR-3000 series, Keyence) was used (Figure 1d). The growth kinetics of the CNT forest was obtained by real-time monitoring and image processing described in our earlier work.[37] The initial growth rate was defined as the growth rate during the initial one-third part of the entire catalytic lifetime. Here, the catalytic lifetime is defined as the period from the start of growth up to the point in time at which the CNT forest height suddenly stops increasing, as shown in Figure S1. This is consistent with the abrupt nature of self-termination that was explained in our previous work by the collective growth model.[10,38−40]

2.3. Characterization of the Alumina Layer and Catalyst Nanoparticles. The surface morphology of the alumina layer was characterized by atomic force microscopy (AFM) using Veeco Dimension 3100 V. The size distribution and number density of catalyst nanoparticles were also obtained by processing the AFM results. Detailed information on data processing is described in our previous work.[23]

The refractive index of alumina films was analyzed using a Horiba Jobin Yvon UVISEL spectroscopic phase-modulated ellipsometer with an incidence angle of 70° and within 1.24−4.13 eV. DeltaPsi2 software was used to fit the obtained data (angles Ψ and Δ) using a model of the system with initially estimated parameters for each layer in the model. The goodness of the fit was assessed by χ^2 values.

To analyze the crystal structure, a Bruker D8 Discover X-ray diffraction (XRD) system was used in the grazing incidence mode within the range of 15−58° and with a fixed incident angle of 5°.

To perform nanoindentation, a Hysitron TI 950 Triboindenter was used with a Berkovich indenter. A loading rate of 1 nm/s was used to create indentations with 10 nm depth.

The contact angles of water, formamide, and diiodomethane droplets on alumina layers with three different annealing conditions (as-deposited, annealed at 700 °C, and annealed at 900 °C) were measured using a Biolin Scientific Optical Tensiometer with the software OneAttention for data analysis. The average and standard deviation of three droplets were recorded for each condition.

3. RESULTS AND DISCUSSION

3.1. Effect of T_c on Forest Height and Properties of CNTs. The final height of an as-grown CNT forest is determined by both the growth rate and the lifetime of the catalyst. In conventional coupled recipes where T_c and T_g are identical or coupled, it is well known that the final height of CNT forests depends on the temperature. While increasing this coupled temperature can increase the growth rate (according to the Arrhenius relationship), it can also cause earlier growth termination, owing to the accelerated deactivation mechanisms such as catalyst nanoparticle ripening. Hence, our decoupled growth approach enables investigating the decoupled effect of T_c on the final height of the CNT forest, which was previously inaccessible in coupled recipes. Importantly, owing to the preheater in our custom-designed reactor, our systematic study of the effect of T_c is also unique because we keep the preheater temperature the same, and hence, we effectively eliminate other extraneous factors, such as the dependence of CNT growth on thermal gas decomposition.

With our decoupled growth recipes, wherein T_c and T_g can be independently controlled, we successfully grew CNT forests. TEM imaging in Figure S2 shows that the synthesized CNTs were multiwalled CNTs (MWCNTs), and the detailed statistics for measurements of outer diameters of CNTs and the number of walls are provided in Table S1. Results show that the mode of distribution of the number of walls was largely the same at 4 for different combinations of T_c and T_g. On the other hand, there was a slight increase in the diameter of CNTs grown at higher T_c (900 °C) compared to those grown at a lower T_c (700 °C) for the same T_g (700 °C). This is attributed to the higher atomic mobility at higher catalyst-treatment temperatures, which promotes diffusion-driven particle coarsening, such as by Ostwald ripening.

For investigating the quality of CNTs, Raman spectra (shown in Figure S3) were also obtained from both top surface and sidewalls of CNT forests grown at various combinations of T_c and T_g. Analysis of I_G/I_D ratios, shown in Figure S3c,d,f, demonstrates that the structural quality of CNTs does not

https://doi.org/10.1021/acs.chemmater.0c04692
Chem. Mater. 2021, 33, 6277−6289

depend on T_c, whereas it depends on T_g. This observed improvement of CNT quality by increasing T_g is due to the enhanced defect-annealing capabilities at higher growth temperatures. Moreover, our results show similar values and trends of I_G/I_D regardless of whether measurements are obtained from the top surface or the sidewalls of the forest.

Regarding the density of CNTs grown at different combinations of T_c and T_g, our results show that density does not depend on T_c, as shown in Figure S4, although the CNT density decreased by increasing T_g. We have previously demonstrated that this finding stems from the T_g-dependence of catalytic activation percentage (or CNT nucleation success rate among the large population of catalyst nanoparticles).[23] Hence, based on all measurements discussed above, T_c does not significantly affect the CNT density, structural quality, or size/geometry.

On the other hand, as we analyze the height measurements of CNT forests grown at various combinations of T_c and T_g, as shown in Figure 2a, there are two important observations worth focusing on. First, at different T_c, the range of T_g where the growth of a CNT forest was possible was different. For example, when T_c was 500 °C, the height was almost 0 at T_g = 720 °C, while growth at T_g = 720 °C was possible when T_c was higher. Second, a higher T_c in general led to a taller CNT forest. This trend is clearly observed when we compare the effect of T_c on forest height at various constant values of T_g (Figure 2b–f). For all T_g values from 650 to 750 °C, the height increased with T_c.

3.2. Effect of T_c on Growth Kinetics. To investigate how changing T_c affects the final height of CNT forests, we analyzed the growth kinetics of each CNT forest that was grown at the same T_g (720 °C) but at different T_c. The reason we chose T_g = 720 °C was because it allows us to obtain the growth results from a wide range of T_c, from 500 to 900 °C, while maintaining the same short transition time of 20 s to rapidly change the temperature from T_c to T_g. Each growth of CNT forest was monitored and recorded to obtain *in situ* growth kinetics as exemplified in Figure 3a.[37,41] Through image processing, the growth curve of each CNT forest was plotted (Figure 3b), from which the growth rate and catalytic lifetime were obtained. The data obtained from T_c = 500 °C were not included in Figure 3 because the CNTs grown at this condition were too short to obtain meaningful growth curves using the optical videography techniques we developed for *in situ* measurements of kinetics.

It is known that the growth rate changes over time during CNT growth.[42−44] Hence, for a meaningful comparison of growth rates, we compared the initial growth rates. In Figure 3c, we observed no significant difference in the initial growth rate at various T_c values. Instead, the catalytic lifetime increased with T_c (Figure 3d). Thus, the increased height with T_c can be mainly attributed to the increased catalytic lifetime, rather than the increased growth rate.

3.3. Effect of T_c on the Evolution of Catalyst Nanoparticle Distribution. How can we interpret the increase of catalytic lifetime with increasing T_c? It is generally accepted that the termination of the collective growth of CNT forests is caused by the accumulation of loss of active catalyst nanoparticles.[39,45] So far, several mechanisms by which each catalyst nanoparticle is deactivated have been proposed and demonstrated. These include carbon overcoating,[46] formation of an inactive phase,[15] and loss of nanoparticles by various

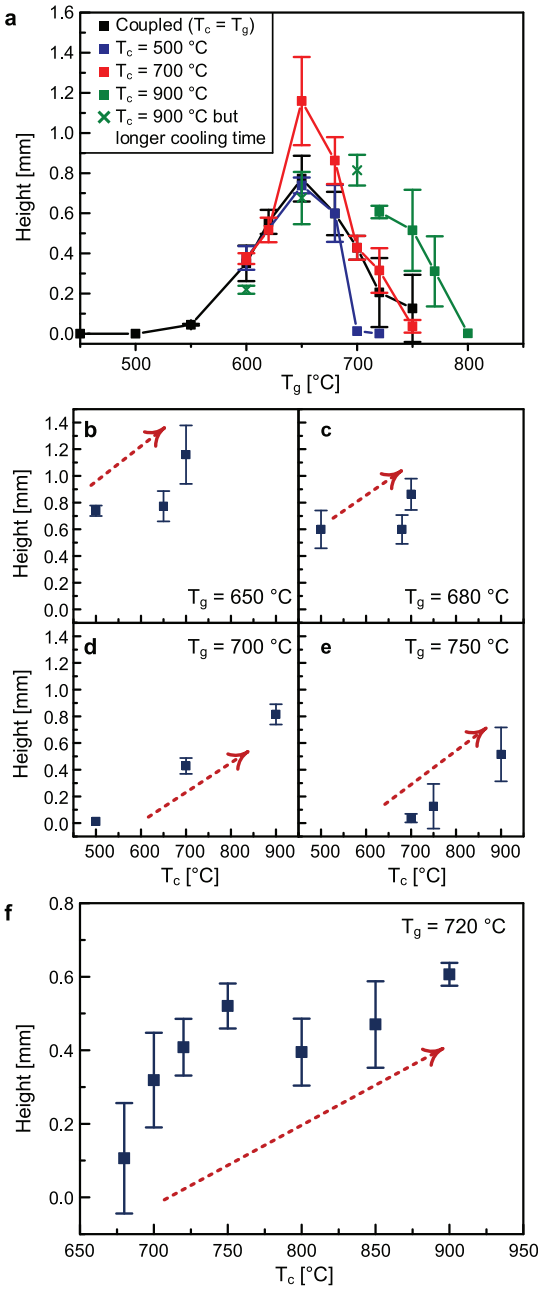

Figure 2. Effect of T_c and T_g on the height of the CNT forest. (a) Heights of the CNT forest at various combinations of T_c and T_g. (b–f) Heights of the CNT forest at various T_c and constant T_g: (b) T_g = 650 °C, (c) T_g = 680 °C, (d) T_g = 700 °C, (e) T_g = 750 °C, and (f) T_g = 720 °C. The error bars were obtained from multiple growth runs (n = 3).

migrations such as Ostwald ripening,[20] subsurface diffusion,[21] and upward migration.[22]

Among these possibilities, it is unlikely that T_c would influence the rate of carbon overcoating or formation of an inactive phase, as these phenomena occur during the growth stage and thus may depend on T_g and not T_c. On the other hand, the migration of the catalyst on the substrate is affected by the interactions between catalyst nanoparticles and the support layer (in this study, alumina),[12] which is dependent on the surface and bulk properties of the supporting oxide. Since the phase, morphology, and surface energy of alumina may evolve during the catalyst formation step, we hypothesize that

https://doi.org/10.1021/acs.chemmater.0c04692
Chem. Mater. 2021, 33, 6277−6289

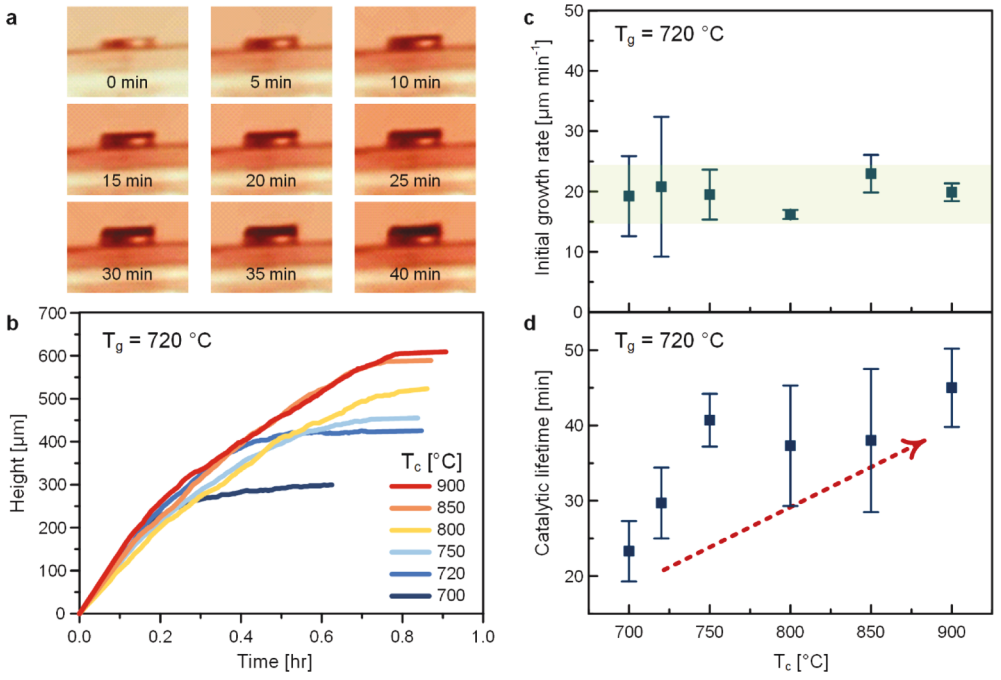

Figure 3. Growth kinetics of the CNT forest. (a) Screenshots of a CNT forest growing inside the reactor (T_c = 900 °C and T_g = 720 °C). (b) Growth curves, (c) initial growth rate, and (d) catalytic lifetime of CNT forests that were grown at the same T_g = 720 °C but various T_c values. The error bars were obtained from multiple growth runs (n = 3).

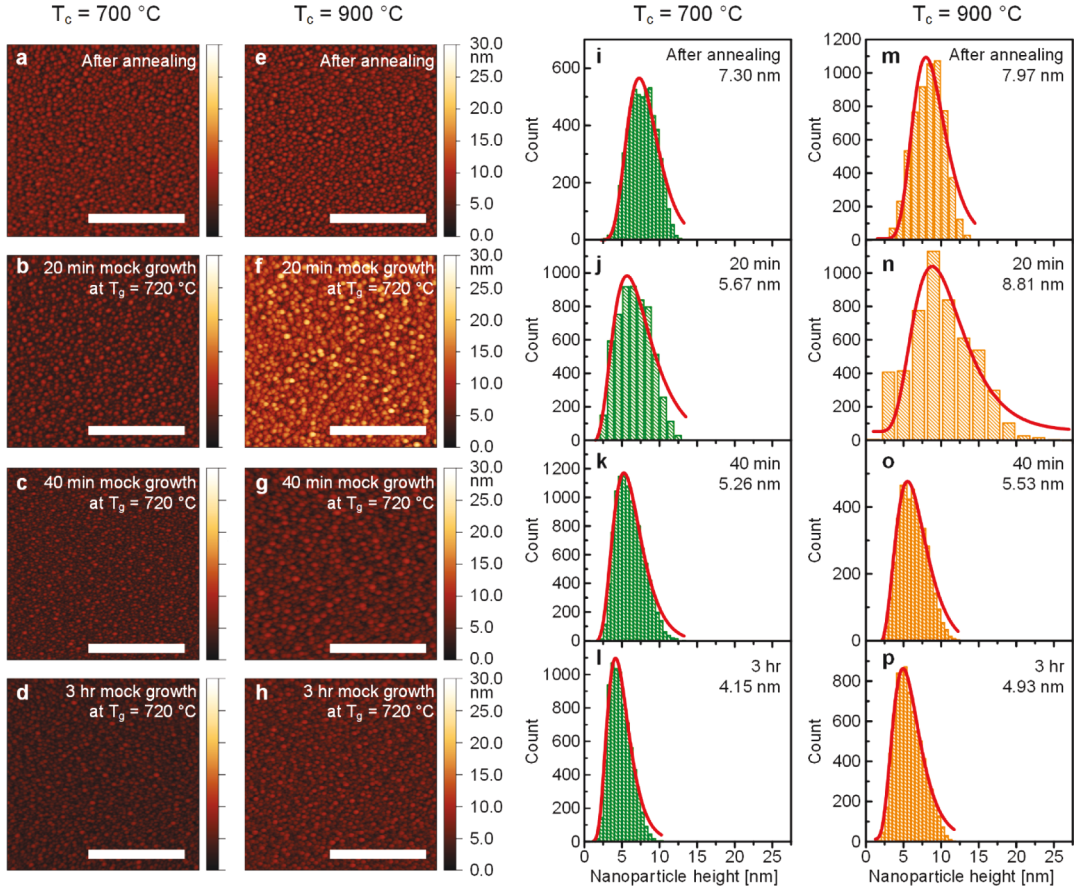

Figure 4. (a–h) AFM images of Fe nanoparticles on the substrate after mock growths for various durations with (i–p) corresponding distributions of nanoparticle height (solid red lines are lognormal fits). The scale bars in (a–h) are 500 nm. The modes of nanoparticle height are inserted as insets in (i–p).

https://doi.org/10.1021/acs.chemmater.0c04692
Chem. Mater. 2021, 33, 6277–6289

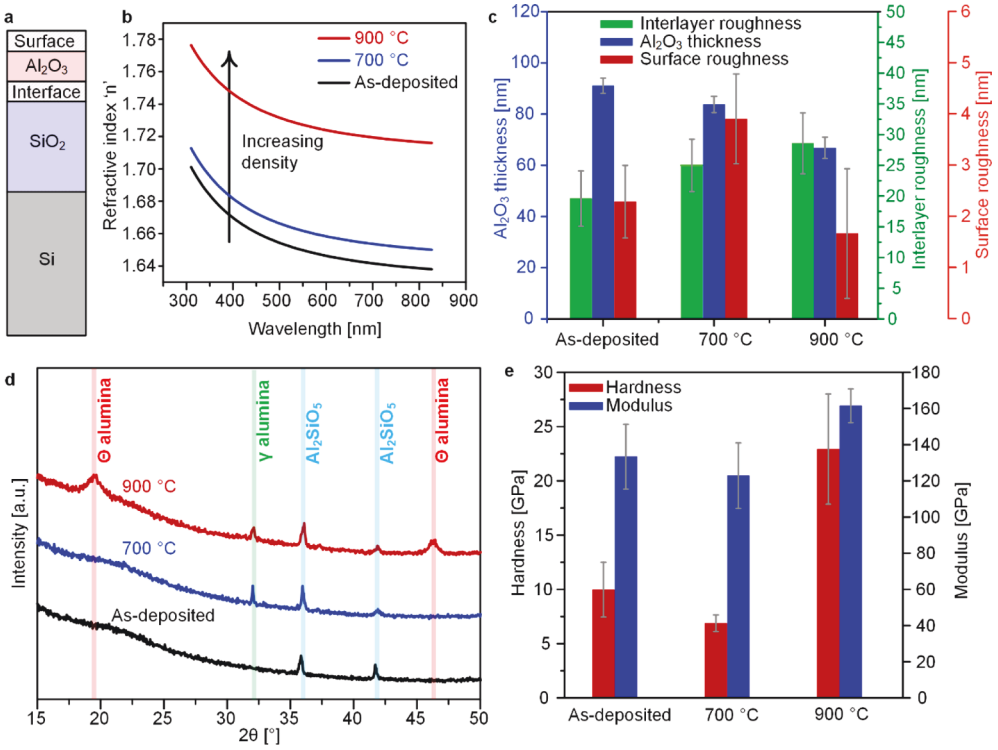

Figure 5. (a) Schematic of the optical model used to fit experimental data with the Sellmeier dispersion formula to obtain the dispersion of refractive index plotted in (b) for Al_2O_3 films with different annealing conditions. (c) Effect of annealing on the thickness, surface roughness, and interface roughness of Al_2O_3 films. (d) XRD spectra for the as-deposited and annealed ALD-Al_2O_3 films show the appearance of crystalline alumina phases after annealing. The phases are based on the reference data shown in Figure S8. (e) Effect of annealing on the hardness and modulus of Al_2O_3 films obtained by nanoindentation.

the boost in the catalytic lifetime (delay in catalytic deactivation) observed for higher T_c results from the modification of alumina layer properties during the catalyst formation step in such a way that hinders the diffusion-derived deactivation mechanisms.

To test this hypothesis, we first analyzed the evolution of the distribution of nanoparticle sizes under mock growth conditions (same as growth but without the hydrocarbon gas) using height measurements from AFM. If the hypothesis is correct, the evolution of size distribution is expected to correlate with the observed growth behavior. We performed mock growth experiments at two T_c (700 °C and 900 °C) at the same T_g (720 °C) for four different durations: 0 min, 20 min, 40 min, and 3 h. The surface of these samples was analyzed by AFM, as shown in Figure 4a–h. The reason we selected 20 min was that it was close to the catalytic lifetime at T_c = 700 °C, while it was obviously shorter than the lifetime at T_c = 900 °C. Thus, after 20 min of mock growth, a marked difference was expected between the samples prepared at different T_c values. 40 min was close to the lifetime at T_c = 900 °C; so, the comparison between 20 and 40 min mock growths at T_c = 900 °C can provide clear insights into how well the observed growth behavior can be explained by the evolution of nanoparticle size distribution. For the comparison of the distributions of the heights of nanoparticles, we used the mode instead of the mean because it is a better representative value, given the skewness of the distributions shown in Figure 4.

After annealing (0 min mock growth), the number densities of Fe nanoparticles were almost similar: 1856 μm^{-2} at T_c = 700 °C and 1987 μm^{-2} at T_c = 900 °C. When T_c was 700 °C, the mode monotonously decreased with the increased mock growth time. The mode was 7.30 nm after annealing (Figure 4i), but it decreased to 5.67 nm after 20 min of mock growth (Figure 4j) and further decreased to 5.26 nm after 40 min (Figure 4k) and to 4.2 nm after 3 h (Figure 4l). On the other hand, when T_c was 900 °C, the distribution of the nanoparticle height evolved in a different way. The mode was 7.97 nm after annealing (Figure 4m), but it increased to 8.81 nm (Figure 4n) after 20 min of mock growth. In addition, at this point, the distribution became much wider, which was quantified by the increase of standard deviation from 2.45 nm after annealing to 4.31 nm after 20 min of mock growth. As the mock growth time got longer than 20 min, the particles became smaller; the mode decreased to 5.53 nm after 40 min (Figure 4o) and to 4.93 nm after 3 h (Figure 4p). The statistics of the mode of nanoparticle height distribution and details of lognormal fits are given in Table S2.

The reduction of the mode with increased mock growth time indicates that a significant portion of Fe catalyst is lost from the surface of the substrate as a result of subsurface diffusion; the nanoparticles migrate into the alumina supporting layer.[21] When T_c was 700 °C, a subsurface diffusion phenomenon began at the early stage of the growth. On the other hand, when T_c was 900 °C, the observed increase in both the mode and the standard deviation of the nanoparticle height after 20 min could be attributed to the Ostwald ripening, wherein larger nanoparticles grow bigger at the expense of smaller nanoparticles that become even smaller with time.[47] Thus, our AFM results indicate that at higher T_c values, subsurface diffusion is significantly slower, which delays growth termination resulting from excessive loss of catalyst. Accordingly, for T_c = 900 °C, Ostwald ripening seemed to dominate

https://doi.org/10.1021/acs.chemmater.0c04692
Chem. Mater. 2021, 33, 6277–6289

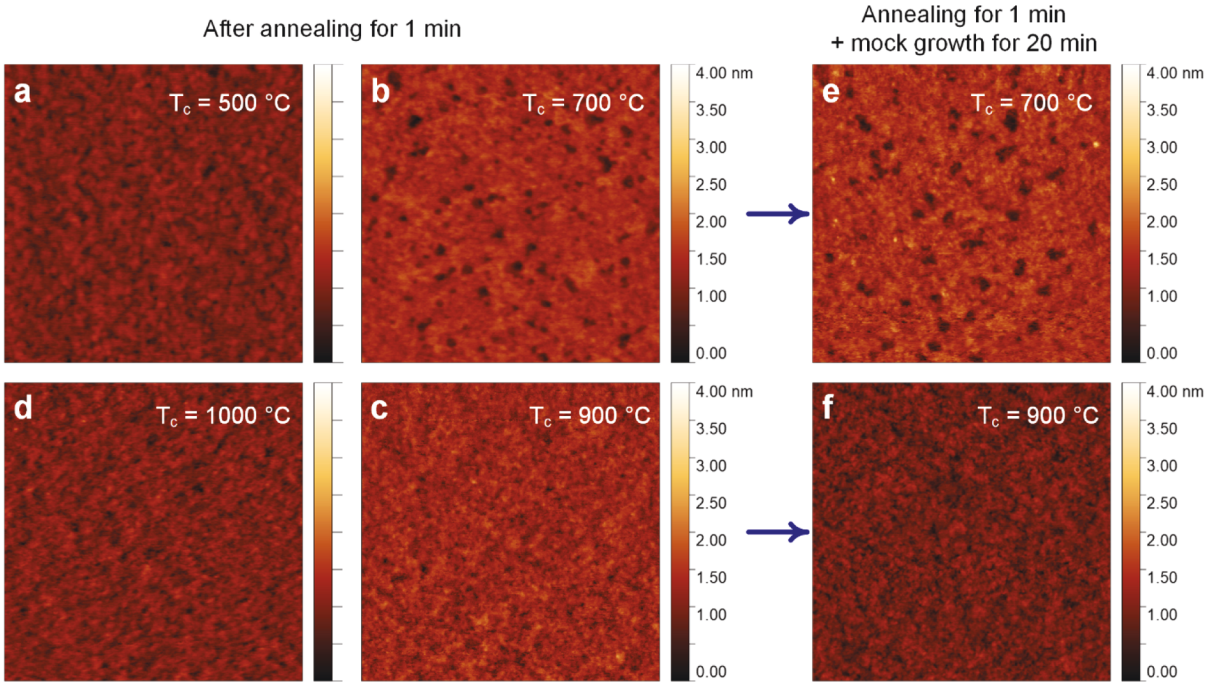

Figure 6. AFM images of the alumina layer surface (a–d) after annealing for 1 min at T_c = (a) 500, (b) 700, (c) 900, and (d) 1000 °C and after annealing for 1 min at T_c = (e) 700 and (f) 900 °C, followed by mock growth at 720 °C for 20 min.

at the early stages of growth (Figure 4f), during which the catalyst mass was largely conserved. At later stages of growth, however, subsurface diffusion eventually dominated, as evidenced by the significant catalyst loss observed on the surface in Figure 4h. It is worth noting here that the discussion above for nanoparticle size distributions is only used as indirect evidence for differences in subsurface diffusion among samples prepared at T_c values of 700 and 900 °C. Moreover, interpreting these AFM results is also limited by the difference between actual growth and mock growth. In the case of actual CNT growth experiments, wherein a hydrocarbon gas is introduced after the catalyst formation step, there are possibilities for upward diffusion along the length of the CNTs. On the other hand, during our mock growth experiments, wherein no hydrocarbons are introduced and no CNTs grow, this possibility of upward diffusion is eliminated. Hence, more direct characterization techniques of the alumina layer itself are needed to more definitely demonstrate the decoupled effect of T_c on subsurface diffusion.

3.4. Effect of T_c on the Phase, Morphology, and Surface Energy of the Alumina Layer. To further understand why the subsurface diffusion rate was slower when T_c was 900 °C compared to when T_c was 700 °C, we now fully characterize the alumina layer after a mock catalyst formation step (only the alumina without the iron nanocatalyst). In particular, the diffusion rate through a solid thin film depends on its porosity and density (given that all other conditions are equal). Thus, our hypothesis is that the difference in the subsurface diffusion rate is explained by the densification of the alumina layer at higher T_c values. That is, the alumina layer after annealing at T_c = 900 °C is less porous and denser than that at T_c = 700 °C. To test this hypothesis, we combined various characterization techniques to reveal the temperature-dependent evolution of the alumina during the catalyst formation step. We employed ellipsometry, XRD, nanoindentation, AFM, and contact angle measurement to thoroughly investigate the changes to the morphology, density, phase, and surface energy of the alumina layer as a function of T_c. It should be noted that 100 nm thick alumina was used for these measurements mainly to avoid the influence of the substrate on nanoindentation measurements, that is, to make sure that the thickness of the film is at least 10 times larger than the penetration depth or total displacement of the indenter (10 nm in our case). Moreover, using thicker alumina also helped to obtain XRD spectra with a higher signal-to-noise ratio.

3.4.1. Ellipsometry. To gain insights into the evolution of density and film morphology as a function of T_c, we first employed spectroscopic ellipsometry, which is often used to measure the optical properties of thin films to infer their thickness, density, and roughness. As schematically shown in Figure S5, the collected data (angles Ψ and Δ as a function of wavelength) are fitted using an optical model of the system with initial estimated values of the fitting parameters. Therefore, establishing an optical model of the system along with using a proper dispersion formula is necessary for ellipsometry data analysis. As shown in Figure 5a, components to develop an optical model for Al_2O_3 on Si/SiO_2 include Si substrate, SiO_2 oxide layer, Al_2O_3–SiO_2 interlayer,[48] Al_2O_3 layer, and a top layer for surface roughness.[48,49] Choosing the right dispersion formula is important, and various dispersion functions, including Tauc–Lorentz,[49] Sellmeier,[48,50] and Cauchy,[13,51] have been used with Al_2O_3. We used several optical models to fit the data: (1) $Al_2O_3/SiO_2/Si$ with the Sellmeier dispersion model for alumina, (2) $Al_2O_3/SiO_2/Si$ with the Cauchy dispersion model for alumina, (3) surface layer/Al_2O_3/SiO_2–Al_2O_3 interlayer/SiO_2/Si with the Sellmeier dispersion model for alumina, (4) surface layer/$Al_2O_3/SiO_2/Si$ with the Sellmeier dispersion model for alumina, and (5) Al_2O_3/SiO_2–Al_2O_3 interlayer/SiO_2/Si with the Sellmeier dispersion model for alumina. The corresponding fitting curves are presented in Figure S6, and the fitted parameters along

https://doi.org/10.1021/acs.chemmater.0c04692
Chem. Mater. 2021, 33, 6277–6289

with χ^2 values are listed in Tables S3−S7. The refractive index, $n(\lambda)$, is defined by $n(\lambda) = A + \frac{B}{\lambda^2} + \frac{C}{\lambda^4}$ with the Cauchy dispersion model and by $n(\lambda) = \sqrt{A + \frac{B\lambda^2}{\lambda^2 - \lambda_1^2}}$ with the Sellmeier dispersion model, where the fixed values of B = 1.32 and λ_1 = 121.59 nm were used according to the literature.[50,52] In the case of the simple model of the system ($Al_2O_3/SiO_2/Si$) with Sellmeier and Cauchy dispersion functions, the refractive index (n) was calculated and plotted as a function of the wavelength in Figure S7a,b, respectively. Both models show that thermal treatment at 900 °C leads to a noticeable increase in the refractive index, corresponding to an increase in the density of the alumina layer, which agrees with the results reported in the literature. For example, Cimalla et al. showed a noticeable increase in the density of ALD-AlO_x films annealed at 900 °C and confirmed the positive correlation between the refractive index of the films and their density.[48]

We also used a more sophisticated model (Figure 5a) to take into account the roughness of the Al_2O_3−SiO_2 interlayer and the top surface roughness of the alumina layer. Based on the Bruggeman effective medium approximation, a layer of 50% SiO_2 and 50% Al_2O_3 was considered for the interface layer, and a layer with 50% Al_2O_3 and 50% void was assumed for the surface roughness layer. Using this model and the Sellmeier dispersion formula, the refractive index (n) as a function of wavelength is plotted in Figure 5b, and the fitted parameters for Al_2O_3−SiO_2 interlayer roughness, Al_2O_3 thickness, and surface roughness are shown in Figure 5c and Table S5. Interestingly, the calculated thickness of the alumina layer decreased after annealing at 900 °C, which indicates densification. This thickness decrease at 900 °C was also observed when several alternative configurations of layers were used for the optical model, as listed in Tables S3, S4, S6, and S7. Hence, this result does not depend on the model choice, further confirming the densification hypothesis. Moreover, both the increase of the calculated surface roughness values from ellipsometry for the case of 700 °C and decrease for the case of 900 °C, shown in Figure 5c, agree with the experimental AFM results shown in Figure 6. It is worth noting that the similar trends for roughness, obtained by ellipsometry on 100 nm thick alumina and AFM on 10 nm thick alumina, suggest that the findings of these experiments are transferable to the case of 10 nm alumina. The observed increase of the interlayer roughness with temperature can be attributed to the intermixing at the Al_2O_3−SiO_2 interface with high-temperature annealing.[51]

3.4.2. X-ray Diffraction. To examine the effect of different thermal pretreatment temperatures on the phase evolution of the alumina layer, an XRD analysis was performed. It is known that thin alumina films deposited by ALD within a temperature range of 200−300 °C are largely amorphous,[53] and our results in Figure 5d confirm this. As shown in Figure S8h,k, the two peaks at 2θ = 35.8° and 2θ = 41.7° match the peaks from the spectrum of orthorhombic Al_2SiO_5. The formation of an AlO_x−SiO_y phase has been previously documented for the as-prepared plasma-enhanced ALD process of alumina on silicon wafers with a native oxide layer.[54] Moreover, other studies have shown the formation of an interfacial layer during the annealing of ALD-Al_2O_3 on a Si substrate without any oxide layer,[53,55] with a native oxide layer,[54] or with a few-nanometer-thick grown oxide layer.[51,56] According to Lifshits et al.,[57] even with a thin SiO_2 layer, the out-diffusion of Si toward the interface is facilitated at high annealing temperatures owing to imperfections in the oxide. In our case, there is a 300 nm thick oxide layer on the Si substrate, which does not exhibit any strong peaks in the XRD spectrum of the bare SiO_2/Si wafer (Figure S8i) in nontreated and annealed conditions. Hence, the peaks at 2θ = 35.8° and 2θ = 41.7° that appeared for the as-deposited as well as annealed alumina samples (Figure 5d) were assigned to an interfacial AlO_x−SiO_y layer.

Figure 5d also shows that annealing alumina at 700 °C resulted in the appearance of a peak at 2θ = 32° corresponding to the crystallization of the alumina film into a tetragonal γ phase (Figures S8a,d). Further crystallization of alumina was observed at a higher annealing temperature of 900 °C, which was accompanied by the appearance of two more peaks at 2θ = 19.4° and 2θ = 46.4°, corresponding to a monoclinic θ phase (Figures S8c,f). Our results agree with a previous work in the literature, in which the above-mentioned peaks for alumina films were observed with annealing at 800 and 1000 °C in the N_2 atmosphere.[58]

3.4.3. Nanoindentation. As a further confirmation for the above-mentioned observations of denser and more crystalline alumina layers at higher thermal pretreatment temperatures, we use nanoindentation to determine the hardness and modulus of 100 nm thick alumina films on SiO_2/Si as a function of annealing temperature. The load−displacement curves are shown in Figure S9. Hardness and elastic modulus values shown in Figure 5e are calculated from at least four indentations on each sample. As seen in Figure 5e, the highest hardness (22.93 ± 5.07 GPa) and modulus (161.50 ± 9.34 GPa) were achieved for the film annealed at 900 °C. Our results agree with the values reported in the literature with lower hardness for amorphous films and higher values for crystalline films. A review of the literature reveals that hardness values for Al_2O_3 films depend on the deposition method, processing parameters, and the nanoindentation setup, ranging between 4.8 and 20.8 GPa for amorphous films and between 16.3 and 25 GPa for crystalline films.[59−68] Zywitzki and Hoetzch[67] measured the hardness of alumina layers that were deposited on steel substrates by reactive pulsed magnetron sputtering under various processing parameters to form desired phases. In that study, hardness values were correlated to the alumina phase: 9−10 GPa for amorphous, 17−19 GPa for γ-Al_2O_3, and 20−22 GPa for α-Al_2O_3. Balakrishnan et al. showed that the amorphous alumina films deposited by pulse laser deposition at 300 K had a hardness of 20.8 GPa, while the hardness of the γ-Al_2O_3 film deposited at 973 K was 24.7 GPa.[59] Another study by Cheng et al. also reported hardness values ranging from 16.3 GPa for a mixture of γ- and α-alumina phases to 23.8 GPa for α-Al_2O_3.[61] Higher hardness of 25 GPa was also reported for alumina films with predominantly γ-phase.[68] It is noteworthy that our results show a slightly lower hardness and elastic modulus for the alumina film annealed at 700 °C compared to the as-deposited films. This is attributed to the remarkably higher roughness and porosity observed in ellipsometry (Figure 5c) and in AFM imaging (Figure 6b,e).

3.4.4. AFM. We first observed the morphology of the surface of the alumina layer after annealing at various temperatures. The as-deposited sample had a very flat surface (Figure S10). The surface remained flat after annealing at 500 °C, as shown in Figure 6a. Interestingly, after annealing at 700 °C, pits were distributed over the whole area, as shown in Figure 6b. These pits were not observed after annealing at higher annealing

https://doi.org/10.1021/acs.chemmater.0c04692
Chem. Mater. 2021, 33, 6277−6289

temperatures (900 and 1000 °C) (Figure 6c,d). We also performed mock growths at 720 °C for 20 min to observe the pits at T_c = 700 °C and T_c = 900 °C. The pits formed during annealing at 700 °C did not disappear after the mock growth at 720 °C for 20 min (Figure 6e). At T_c = 900 °C, pits were not observed after the mock growth (Figure 6f).

These pits observed at T_c = 700 °C can be understood by drawing an analogy to sinkholes. Sinkholes are caused by various collapses inside a layer. Similarly, when the alumina layer was annealed at 700 °C, internal local densification can cause the formation of pits owing to the localized film pores that form owing to the conservation of mass during this process (i.e., as some parts of the films densify locally, some pores open elsewhere). When the alumina layer was annealed at 900 °C, a denser, more crystalline, and less porous phase was formed. Thus, the morphology of the alumina surface remained flat. Hence, the formation of pits at T_c = 700 °C is consistent with the more porous and less dense alumina phase observed by ellipsometry and nanoindentation (Figure 5).

The density of the alumina support layer has previously been reported to be an important factor in the growth of CNTs. Islam et al. have reported a method to transform a crystal sapphire substrate into an active catalyst support that enables the growth of a CNT forest.[69] They treated the crystal sapphire by argon-ion beam bombardment to make it amorphous and porous. Proper porosity of the alumina layer is required for the CNT growth, but our results imply that excessive porosity would be detrimental by causing subsurface diffusion of catalyst particles. It was also reported that tailoring the density of the alumina support by oxygen plasma treatment prior to the deposition of iron film suppresses the subsurface diffusion and results in the growth of taller and denser CNT forests.[70,71] Yang et al. controlled the density of the alumina supporting layer via thermal annealing and argon-ion beam bombardment.[72] They revealed that thermal annealing densifies the alumina layer and thus prevents subsurface diffusion of the catalyst particles and that ion beam bombardment amorphizes the alumina layer, increasing the porosity, defects, and oxygen-containing functional groups on it to inhibit the Ostwald ripening of catalyst nanoparticles. These results are in agreement with ours. The authors of that study combined the two treatments to engineer the alumina layer but did not investigate the effect of alumina density on the catalytic lifetime as the focus was on controlling the diameter of CNTs. These studies combined with our results indicate that the precise engineering of the alumina layer enables highly controlled growth of CNT forests in terms of sizes (from previous work)[72] and catalytic lifetime (from our work). It is worth noting here that in contrast to previous studies, in which the modification of the alumina layer was achieved in a separate *ex situ* processing step, typically after alumina deposition before catalyst film deposition, our work here demonstrates the ability of tailoring the alumina film *in situ* during the CVD process. Moreover, our work is the first to leverage decoupled growth recipes to tailor the alumina film and the catalytic lifetime via rapid changes of temperature during the dynamically programmed steps in the CVD reactor without requiring any modification in the samples prior to loading them in the CVD reactor.

3.4.5. Contact Angle. Last, we compared the surface properties of alumina layers. The surface properties can be characterized by contact angle measurement. According to the van Oss–Good–Chaudhury model, the surface free-energy components (Lifshitz–van der Waals component and acid–base component) can be determined by solving the Young–Dupre equations by measuring the contact angles using three liquids: two polar and one nonpolar, with known surface free energies.[73] Using this method, Amama et al. recently reported contact angle measurement to compare the surface energies of different types of alumina layers.[74,75] Similarly, we measured the contact angle of an alumina layer subjected to annealing conditions: as-deposited, annealed at 700, and annealed at 900 °C. We used water and formamide as polar liquids and diiodomethane as a nonpolar liquid. The measurements are visually shown in Figure 7a, and the average contact angles are

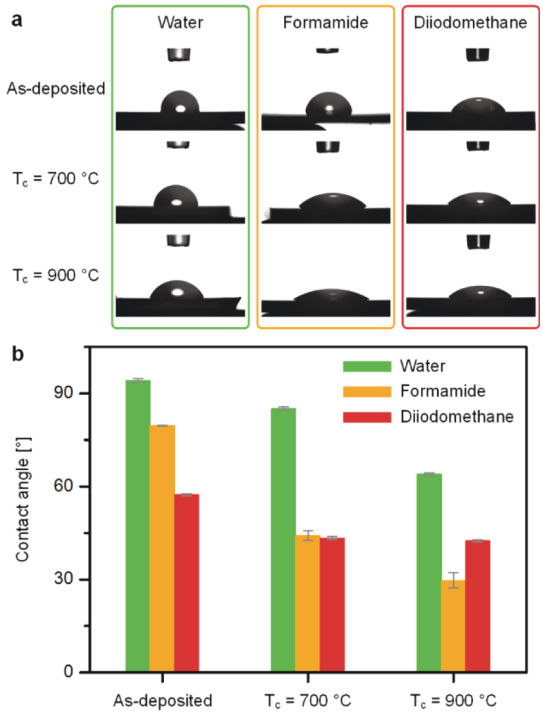

Figure 7. (a) Images of contact angle measurements and (b) corresponding plots of average contact angles.

plotted in Figure 7b. Obviously, different samples showed a noticeable difference in the contact angles, indicating that the alumina layers of the three samples prepared at different annealing conditions have different surface energies.

We quantified the surface energy components by solving the Young–Dupre equation. The calculated surface energy components and total surface energy are summarized in Table 2. The surface free-energy components as well as the total energy were significantly different for the three samples. Thus, the contact angle measurement results also support our

Table 2. Surface Free-Energy Components and the Total Surface Free Energies of Alumina Layers Calculated from the Contact Angle Measurement

	surface free-energy components and total surface free energy (mJ m^{-2})				
substrate	nonpolar	polar, γ^{AB}	acidic, γ^{+}	basic, γ^{-}	γ^{TOT}
as-deposited	30.1	2.17	0.263	4.47	32.3
Tc = 700 °C	30.1	1.76	5.69	0.137	31.8
Tc = 900 °C	38.3	10.2	3.19	8.20	48.6

https://doi.org/10.1021/acs.chemmater.0c04692
Chem. Mater. 2021, 33, 6277–6289

hypothesis that different annealing temperatures lead to different properties of the alumina layer. It is also noteworthy that the Lewis basicity was higher when the sample was annealed at 900 °C than at 700 °C. Amama et al. reported that high Lewis basicity is helpful to the growth of a CNT forest,[74,75] although the mechanism of that improvement was not explained in terms of whether it was because of increased growth rate or catalytic lifetime. Nevertheless, both prior studies and our present work show that taller forests can be grown from the alumina layers with higher Lewis basicity.

3.5. Mechanism Explaining Increased Catalytic Lifetime at Higher T_c. We show that the T_c dependence of catalytic lifetime results from the T_c dependence of the alumina layer density, crystallinity, and surface energy, which collectively control the surface and subsurface diffusion rates. The different subsurface diffusion rates at different T_c values are strongly supported by the various characterization results of alumina layers including ellipsometry, XRD, and nanoindentation, as presented in Figure 5. Accordingly, the different situations of CNT forest growths at two different T_c values (700 and 900 °C) are schematically illustrated in Figure 8. The

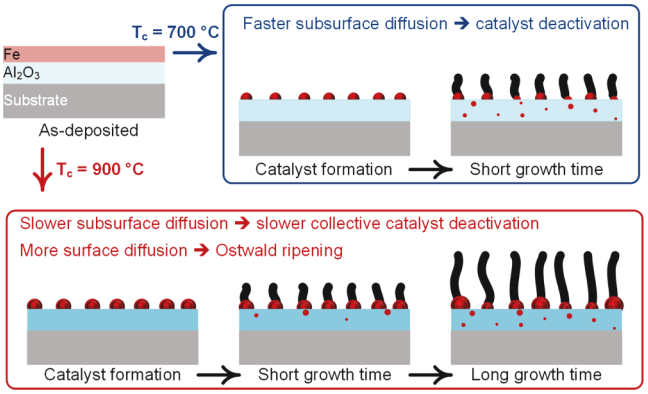

Figure 8. Scheme that explains the evolution of catalyst nanoparticles during the CNT growth after annealing at different T_c values.

alumina layer after annealing at T_c = 900 °C has a higher density and a lower porosity than that at T_c = 700 °C. At T_c = 700 °C, as the result of the higher porosity of the alumina layer, the subsurface diffusion into the alumina layer is faster, and the catalyst loss by this mechanism is dominant in ceasing the overall growth of the CNT forest. When T_c is 900 °C, due to the dense alumina layer, the subsurface diffusion rate is initially so slow that only Ostwald ripening dominates at first. After a prolonged growth time, subsurface diffusion eventually takes over and the growth terminates. We can infer from this result that the massive loss of catalyst by the subsurface diffusion into the alumina layer is the dominant catalyst deactivation mechanism, rather than Ostwald ripening.

Further support to the mechanism explained above is also observed in our additional experiments, where we annealed the as-deposited alumina film at 750 °C (referred to as Alumina-750C) and at 950 °C (referred to as Alumina-950C) prior to Fe deposition. The annealing environment was a mixture of hydrogen and helium that is similar to the conditions during our typical catalyst preparation step. It is noteworthy that CNT forest heights in these additional experiments are generally lower than those presented in Figure 2 because all new experiments were carried out without turning on the preheater (i.e., the preheater is at room temperature), while the rest of the results shown in this paper were obtained at a preheater temperature of 825 °C. The reason the preheater was kept at room temperature for these additional experiments is to focus on surface reactions and avoid the effects of the gas-phase thermal decomposition products on growth. Figure S11 includes more details about the annealing recipe and the results of these experiments. Here, we compare the height of forests grown on these samples to the ones grown on samples with no annealing of alumina prior to Fe deposition (referred to as Alumina-0C). Note that in all these samples, alumina and Fe were deposited in separate deposition runs. As shown in Figure S11a,b, regardless of the growth recipe, shorter forests grew on Alumina-750C and Alumina-950C, compared to the ones that grew on Alumina-0C, showing that annealing the alumina in a separate step before Fe deposition actually results in shorter forests. We used three different growth recipes: the first is a coupled recipe, wherein $T_c = T_g$ = 670 °C, as shown in Figure S11d. The second and the third growth recipes had an additional 1 min rapid thermal pretreatment step of the catalyst. We denote the temperature of this additional rapid pretreatment by T_{preC}, which was set at T_{preC} = 750 °C and T_{preC} = 950 °C for the second and third growth recipes, as shown in Figure S11f,g, respectively. CNT forest height measurements in Figure S11a, indicate that adding a pretreatment at T_{preC} = 750 °C and T_{preC} = 950 °C enhanced the growth height (significantly for the case of T_{preC} = 950 °C). Optical images of the forests grown on Alumina-0C samples (Figure S11e) depict the increase in forest height. Hence, only rapid thermal pretreatment in a closed reactor right before growth can realize the boost to catalytic lifetime that is demonstrated in this work.

4. CONCLUSIONS

In this work, we demonstrate that the lifetime of nanocatalysts used in the CVD growth of CNTs from alumina-supported iron nanoparticles can significantly increase by decoupling the catalyst formation step (during which nanoparticles are formed by solid-state dewetting in a reducing gas environment) from the CNT growth step (during which individual CNTs nucleate and grow from catalytically active nanoparticles in the presence of a hydrocarbon gas). A significant increase in the catalytic lifetime was observed when the catalyst-formation temperature (T_c) was higher than the CNT-growth temperature (T_g). To explain our findings, we analyzed the Fe nanoparticles as well as the support alumina layer after annealing at two T_c values: 700 and 900 °C. AFM analysis of Fe nanoparticles showed that the nanoparticles were lost early on during a mock growth step when T_c was 700 °C, while the subsurface diffusion was substantially postponed when T_c was 900 °C. The characterization of the alumina layer showed that the porosity was lower and the density was higher for films annealed at T_c = 900 °C than at T_c = 700 °C, which is consistent with the slower subsurface diffusion at T_c = 900 °C. The results shed light on the potential of our approach of decoupling each step of CNT growth by CVD using rapid thermal pretreatment in dynamic growth recipes. Moreover, insights from this universally applicable approach can apply to other oxide-supported catalyst systems because the mechanisms of the boosted catalytic lifetime depend on leveraging the thermochemical tunability of the oxide phase, crystallinity, density, and surface energy.

https://doi.org/10.1021/acs.chemmater.0c04692
Chem. Mater. 2021, 33, 6277−6289

■ ASSOCIATED CONTENT

Supporting Information

The Supporting Information is available free of charge at https://pubs.acs.org/doi/10.1021/acs.chemmater.0c04692.

Illustration of catalytic lifetime definition on a representative growth kinetics curve; representative TEM images of CNTs; Raman spectra from the top and sidewall of CNT forests along with IG/ID ratio for structural quality analysis; density dependence on decoupled T_c and T_g; ellipsometry data modeling along with curve fitting and dispersion of the refractive index; XRD results with identification of peaks for different phases of alumina; force−displacement curves from the nanoindentation of alumina films; AFM of the as-deposited alumina films; CNT forest heights showing the effect of annealing alumina prior to Fe deposition as well as the effect of adding an additional pretreatment step prior to growth; statistical analysis of CNT outer diameter and number of walls; statistical analysis of nanoparticle heights from AFM images of samples prepared at different mock growth conditions; and fitted parameters for ellipsometry data based on different multilayer film models according to both Sellmeier and Cauchy dispersion formulas (PDF)

■ AUTHOR INFORMATION

Corresponding Author

Mostafa Bedewy − *Department of Industrial Engineering, University of Pittsburgh, Pittsburgh, Pennsylvania 15261, United States; Department of Chemical and Petroleum Engineering and Department of Mechanical Engineering and Materials Science, University of Pittsburgh, Pittsburgh, Pennsylvania 15261, United States;* orcid.org/0000-0003-4182-7533; Email: mbedewy@pitt.edu

Authors

Jaegeun Lee − *Department of Industrial Engineering, University of Pittsburgh, Pittsburgh, Pennsylvania 15261, United States; School of Chemical Engineering, Pusan National University, Busan 46241, Republic of Korea;* orcid.org/0000-0001-8817-0191

Golnaz Najaf Tomaraei − *Department of Industrial Engineering, University of Pittsburgh, Pittsburgh, Pennsylvania 15261, United States*

Moataz Abdulhafez − *Department of Industrial Engineering, University of Pittsburgh, Pittsburgh, Pennsylvania 15261, United States*

Complete contact information is available at: https://pubs.acs.org/10.1021/acs.chemmater.0c04692

Author Contributions

[⊥]J.L. and G.N.T. contributed equally to this work.

Notes

The authors declare no competing financial interest.

■ ACKNOWLEDGMENTS

This research was supported by the National Science Foundation (NSF) under award number 1825772 (any opinions, findings, and conclusions or recommendations expressed in this material are those of the author(s) and do not necessarily reflect the views of the National Science Foundation). This work was also partially supported by the National Research Foundation of Korea (NRF) grant funded by the Korea government (MSIT) (no. 2020R1G1A1013953). The characterization was performed, in part, at the Nanoscale Fabrication and Characterization Facility, a laboratory of the Gertrude E. and John M. Petersen Institute of NanoScience and Engineering, housed at the University of Pittsburgh and in part at Materials Characterization Laboratory, housed at the Department of Chemistry in the University of Pittsburgh.

■ REFERENCES

(1) Hata, K.; Futaba, D. N.; Mizuno, K.; Namai, T.; Yumura, M.; Iijima, S. Water-Assisted Highly Efficient Synthesis of Impurity-Free Single-Walled Carbon Nanotubes. *Science* **2004**, *306*, 1362−1364.

(2) Yasuda, S.; Futaba, D. N.; Yamada, T.; Satou, J.; Shibuya, A.; Takai, H.; Arakawa, K.; Yumura, M.; Hata, K. Improved and Large Area Single-Walled Carbon Nanotube Forest Growth by Controlling the Gas Flow Direction. *ACS Nano* **2009**, *3*, 4164−4170.

(3) Cho, W.; Schulz, M.; Shanov, V. Growth and Characterization of Vertically Aligned Centimeter Long CNT Arrays. *Carbon* **2014**, *72*, 264−273.

(4) Lee, J.; Oh, E.; Kim, T.; Sa, J.-H.; Lee, S.-H.; Park, J.; Moon, D.; Kang, I. S.; Kim, M. J.; Kim, S. M.; et al. The Influence of Boundary Layer on the Growth Kinetics of Carbon Nanotube Forests. *Carbon* **2015**, *93*, 217−225.

(5) Lee, C.-H.; Lee, J.; Park, J.; Lee, E.; Kim, S. M.; Lee, K.-H. Rationally Designed Catalyst Layer toward "Immortal" Growth of Carbon Nanotube Forest: Fe Ion Implanted Substrates. *Carbon* **2019**, *152*, 482−488.

(6) Zhang, R.; Zhang, Y.; Zhang, Q.; Xie, H.; Qian, W.; Wei, F. Growth of Half-Meter Long Carbon Nanotubes Based on Schulz-Flory Distribution. *ACS Nano* **2013**, *7*, 6156−6161.

(7) Tsentalovich, D. E.; Headrick, R. J.; Mirri, F.; Hao, J.; Behabtu, N.; Young, C. C.; Pasquali, M. Influence of Carbon Nanotube Characteristics on Macroscopic Fiber Properties. *ACS Appl. Mater. Interfaces* **2017**, *9*, 36189−36198.

(8) Morançais, A.; Caussat, B.; Kihn, Y.; Kalck, P.; Plee, D.; Gaillard, P.; Bernard, D.; Serp, P. A Parametric Study of the Large Scale Production of Multi-Walled Carbon Nanotubes by Fluidized Bed Catalytic Chemical Vapor Deposition. *Carbon* **2007**, *45*, 624−635.

(9) Chen, Z.; Kim, D. Y.; Hasegawa, K.; Osawa, T.; Noda, S. Over 99.6 Wt%-Pure, Sub-Millimeter-Long Carbon Nanotubes Realized by Fluidized-Bed with Careful Control of the Catalyst and Carbon Feeds. *Carbon* **2014**, *80*, 339−350.

(10) Bedewy, M.; Viswanath, B.; Meshot, E. R.; Zakharov, D. N.; Stach, E. A.; Hart, A. J. Measurement of the Dewetting, Nucleation, and Deactivation Kinetics of Carbon Nanotube Population Growth by Environmental Transmission Electron Microscopy. *Chem. Mater.* **2016**, *28*, 3804.

(11) Aziz Ezzat, A.; Bedewy, M. Machine Learning for Revealing Spatial Dependence among Nanoparticles: Understanding Catalyst Film Dewetting via Gibbs Point Process Models. *J. Phys. Chem. C* **2020**, *124*, 27479−27494.

(12) Mattevi, C.; Wirth, C. T.; Hofmann, S.; Blume, R.; Cantoro, M.; Ducati, C.; Cepek, C.; Knop-Gericke, A.; Milne, S.; Castellarin-Cudia, C.; et al. In-Situ X-Ray Photoelectron Spectroscopy Study of Catalyst−Support Interactions and Growth of Carbon Nanotube Forests. *J. Phys. Chem. C* **2008**, *112*, 12207−12213.

(13) Amama, P. B.; Pint, C. L.; Kim, S. M.; McJilton, L.; Eyink, K. G.; Stach, E. A.; Hauge, R. H.; Maruyama, B. Influence of Alumina Type on the Evolution and Activity of Alumina-Supported Fe Catalysts in Single-Walled Carbon Nanotube Carpet Growth. *ACS Nano* **2010**, *4*, 895−904.

(14) Noda, S.; Hasegawa, K.; Sugime, H.; Kakehi, K.; Zhang, Z.; Maruyama, S.; Yamaguchi, Y. Millimeter-Thick Single-Walled Carbon Nanotube Forests: Hidden Role of Catalyst Support. *Jpn. J. Appl. Phys., Part 2* **2007**, *46*, L399.

(15) Mazzucco, S.; Wang, Y.; Tanase, M.; Picher, M.; Li, K.; Wu, Z.; Irle, S.; Sharma, R. Direct Evidence of Active and Inactive Phases of

Fe Catalyst Nanoparticles for Carbon Nanotube Formation. *J. Catal.* **2014**, *319*, 54−60.
(16) Wirth, C. T.; Bayer, B. C.; Gamalski, A. D.; Esconjauregui, S.; Weatherup, R. S.; Ducati, C.; Baehtz, C.; Robertson, J.; Hofmann, S. The Phase of Iron Catalyst Nanoparticles during Carbon Nanotube Growth. *Chem. Mater.* **2012**, *24*, 4633−4640.
(17) Stadermann, M.; Sherlock, S. P.; In, J.-B.; Fornasiero, F.; Park, H. G.; Artyukhin, A. B.; Wang, Y.; De Yoreo, J. J.; Grigoropoulos, C. P.; Bakajin, O.; et al. Mechanism and Kinetics of Growth Termination in Controlled Chemical Vapor Deposition Growth of Multiwall Carbon Nanotube Arrays. *Nano Lett.* **2009**, *9*, 738−744.
(18) Balakrishnan, V.; Bedewy, M.; Meshot, E. R.; Pattinson, S. W.; Polsen, E. S.; Laye, F.; Zakharov, D. N.; Stach, E. A.; Hart, A. J. Real-Time Imaging of Self-Organization and Mechanical Competition in Carbon Nanotube Forest Growth. *ACS Nano* **2016**, *10*, 11496−11504.
(19) Bedewy, M.; Hart, A. J. Mechanical Coupling Limits the Density and Quality of Self-Organized Carbon Nanotube Growth. *Nanoscale* **2013**, *5*, 2928.
(20) Amama, P. B.; Pint, C. L.; McJilton, L.; Kim, S. M.; Stach, E. A.; Murray, P. T.; Hauge, R. H.; Maruyama, B. Role of Water in Super Growth of Single-Walled Carbon Nanotube Carpets. *Nano Lett.* **2009**, *9*, 44−49.
(21) Kim, S. M.; Pint, C. L.; Amama, P. B.; Zakharov, D. N.; Hauge, R. H.; Maruyama, B.; Stach, E. A. Evolution in Catalyst Morphology Leads to Carbon Nanotube Growth Termination. *J. Phys. Chem. Lett.* **2010**, *1*, 918−922.
(22) Jeong, S.; Lee, J.; Kim, H.-C.; Hwang, J. Y.; Ku, B.-C.; Zakharov, D. N.; Maruyama, B.; Stach, E. A.; Kim, S. M. Direct Observation of Morphological Evolution of a Catalyst during Carbon Nanotube Forest Growth: New Insights into Growth and Growth Termination. *Nanoscale* **2016**, *8*, 2055−2062.
(23) Lee, J.; Abdulhafez, M.; Bedewy, M. Decoupling Catalyst Dewetting, Gas Decomposition, and Surface Reactions in Carbon Nanotube Forest Growth Reveals Dependence of Density on Nucleation Temperature. *J. Phys. Chem. C* **2019**, *123*, 28726−28738.
(24) Lee, C. J.; Son, K. H.; Park, J.; Yoo, J. E.; Huh, Y.; Lee, J. Y. Low Temperature Growth of Vertically Aligned Carbon Nanotubes by Thermal Chemical Vapor Deposition. *Chem. Phys. Lett.* **2001**, *338*, 113−117.
(25) Jeong, H. J.; Jeong, S. Y.; Shin, Y. M.; Han, J. H.; Lim, S. C.; Eum, S. J.; Yang, C. W.; Kim, N. G.; Park, C. Y.; Lee, Y. H. Dual-Catalyst Growth of Vertically Aligned Carbon Nanotubes at Low Temperature in Thermal Chemical Vapor Deposition. *Chem. Phys. Lett.* **2002**, *361*, 189−195.
(26) Pint, C. L.; Pheasant, S. T.; Pasquali, M.; Coulter, K. E.; Schmidt, H. K.; Hauge, R. H. Synthesis of High Aspect-Ratio Carbon Nanotube "Flying Carpets" from Nanostructured Flake Substrates. *Nano Lett.* **2008**, *8*, 1879−1883.
(27) Meshot, E. R.; Plata, D. L.; Tawfick, S.; Zhang, Y.; Verploegen, E. A.; Hart, A. J. Engineering Vertically Aligned Carbon Nanotube Growth by Decoupled Thermal Treatment of Precursor and Catalyst. *ACS Nano* **2009**, *3*, 2477−2486.
(28) Nessim, G. D.; Seita, M.; O'Brien, K. P.; Hart, A. J.; Bonaparte, R. K.; Mitchell, R. R.; Thompson, C. V. Low Temperature Synthesis of Vertically Aligned Carbon Nanotubes with Electrical Contact to Metallic Substrates Enabled by Thermal Decomposition of the Carbon Feedstock. *Nano Lett.* **2009**, *9*, 3398−3405.
(29) Zhong, G.; Hofmann, S.; Yan, F.; Telg, H.; Warner, J. H.; Eder, D.; Thomsen, C.; Milne, W. I.; Robertson, J. Acetylene: A Key Growth Precursor for Single-Walled Carbon Nanotube Forests. *J. Phys. Chem. C* **2009**, *113*, 17321−17325.
(30) Nessim, G. D.; Seita, M.; Plata, D. L.; O'Brien, K. P.; John Hart, A.; Meshot, E. R.; Reddy, C. M.; Gschwend, P. M.; Thompson, C. V. Precursor Gas Chemistry Determines the Crystallinity of Carbon Nanotubes Synthesized at Low Temperature. *Carbon* **2011**, *49*, 804−810.
(31) Sugime, H.; Noda, S. Cold-Gas Chemical Vapor Deposition to Identify the Key Precursor for Rapidly Growing Vertically-Aligned Single-Wall and Few-Wall Carbon Nanotubes from Pyrolyzed Ethanol. *Carbon* **2012**, *50*, 2953−2960.
(32) Youn, S. K.; Frouzakis, C. E.; Gopi, B. P.; Robertson, J.; Teo, K. B. K.; Park, H. G. Temperature Gradient Chemical Vapor Deposition of Vertically Aligned Carbon Nanotubes. *Carbon* **2013**, *54*, 343−352.
(33) Yang, N.; Youn, S. K.; Frouzakis, C. E.; Park, H. G. An Effect of Gas-Phase Reactions on the Vertically Aligned CNT Growth by Temperature Gradient Chemical Vapor Deposition. *Carbon* **2018**, *130*, 607−613.
(34) Sakurai, S.; Inaguma, M.; Futaba, D. N.; Yumura, M.; Hata, K. Diameter and Density Control of Single-Walled Carbon Nanotube Forests by Modulating Ostwald Ripening through Decoupling the Catalyst Formation and Growth Processes. *Small* **2013**, *9*, 3584−3592.
(35) Sakurai, S.; Inaguma, M.; Futaba, D.; Yumura, M.; Hata, K. A Fundamental Limitation of Small Diameter Single-Walled Carbon Nanotube Synthesis-a Scaling Rule of the Carbon Nanotube Yield with Catalyst Volume. *Materials* **2013**, *6*, 2633−2641.
(36) Li, J.; Bedewy, M.; White, A. O.; Polsen, E. S.; Tawfick, S.; Hart, A. J. Highly Consistent Atmospheric Pressure Synthesis of Carbon Nanotube Forests by Mitigation of Moisture Transients. *J. Phys. Chem. C* **2016**, *120*, 11277−11287.
(37) Abdulhafez, M.; Lee, J.; Bedewy, M. In Situ Measurement of Carbon Nanotube Growth Kinetics in a Rapid Thermal Chemical Vapor Deposition Reactor With Multizone Infrared Heating. *J. Micro Nano-Manuf.* **2020**, *8*, 010902.
(38) Meshot, E. R.; Hart, A. J. Abrupt Self-Termination of Vertically Aligned Carbon Nanotube Growth. *Appl. Phys. Lett.* **2008**, *92*, 113107.
(39) Bedewy, M.; Meshot, E. R.; Guo, H.; Verploegen, E. A.; Lu, W.; Hart, A. J. Collective Mechanism for the Evolution and Self-Termination of Vertically Aligned Carbon Nanotube Growth. *J. Phys. Chem. C* **2009**, *113*, 20576.
(40) Bedewy, M.; Meshot, E. R.; Reinker, M. J.; Hart, A. J. Population Growth Dynamics of Carbon Nanotubes. *ACS Nano* **2011**, *5*, 8974−8989.
(41) Lee, J.; Abdulhafez, M.; Bedewy, M. Multizone Rapid Thermal Processing to Overcome Challenges in Carbon Nanotube Manufacturing by Chemical Vapor Deposition. *J. Manuf. Sci. Eng.* **2019**, *141*, 091006.
(42) Zhu, L.; Hess, D. W.; Wong, C.-P. Monitoring Carbon Nanotube Growth by Formation of Nanotube Stacks and Investigation of the Diffusion-Controlled Kinetics. *J. Phys. Chem. B* **2006**, *110*, 5445−5449.
(43) Futaba, D. N.; Hata, K.; Yamada, T.; Mizuno, K.; Yumura, M.; Iijima, S. Kinetics of Water-Assisted Single-Walled Carbon Nanotube Synthesis Revealed by a Time-Evolution Analysis. *Phys. Rev. Lett.* **2005**, *95*, 056104.
(44) Puretzky, A. A.; Geohegan, D. B.; Jesse, S.; Ivanov, I. N.; Eres, G. In Situ Measurements and Modeling of Carbon Nanotube Array Growth Kinetics during Chemical Vapor Deposition. *Appl. Phys. A* **2005**, *81*, 223−240.
(45) Bedewy, M.; Meshot, E.; Reinker, M.; Hart, A. J. Population growth dynamics of carbon nanotubes. *ACS Nano* **2011**, *5*, 8974−8989.
(46) Yamada, T.; Maigne, A.; Yudasaka, M.; Mizuno, K.; Futaba, D. N.; Yumura, M.; Iijima, S.; Hata, K. Revealing the Secret of Water-Assisted Carbon Nanotube Synthesis by Microscopic Observation of the Interaction of Water on the Catalysts. *Nano Lett.* **2008**, *8*, 4288−4292.
(47) Voorhees, P. W. The Theory of Ostwald Ripening. *J. Stat. Phys.* **1985**, *38*, 231−252.
(48) Cimalla, V.; Baeumler, M.; Kirste, L.; Prescher, M.; Christian, B.; Passow, T.; Benkhelifa, F.; Bernhardt, F.; Eichapfel, G.; Himmerlich, M.; Krischok, S.; Pezoldt, J. Densification of Thin Aluminum Oxide Films by Thermal Treatments. *Mater. Sci. Appl.* **2014**, *05*, 628−638.
(49) Shi, S.; Qian, S.; Hou, X.; Mu, J.; He, J.; Chou, X. Structural and Optical Properties of Amorphous Al2O3 Thin Film Deposited by

https://doi.org/10.1021/acs.chemmater.0c04692
Chem. Mater. 2021, 33, 6277−6289

Atomic Layer Deposition. *Adv. Condens. Matter Phys.* **2018**, *2018*, 7598978.
(50) Barbos, C.; Blanc-Pelissier, D.; Fave, A.; Botella, C.; Regreny, P.; Grenet, G.; Blanquet, E.; Crisci, A.; Lemiti, M. Al2O3 Thin Films Deposited by Thermal Atomic Layer Deposition: Characterization for Photovoltaic Applications. *Thin Solid Films* **2016**, *617*, 108−113.
(51) Hsain, Z.; Zeng, G.; Strandwitz, N. C.; Krick, B. A. Wear Behavior of Annealed Atomic Layer Deposited Alumina. *Wear* **2017**, *372*−*373*, 139−144.
(52) Kumar, P.; Wiedmann, M. K.; Winter, C. H.; Avrutsky, I. Optical Properties of Al2O3 Thin Films Grown by Atomic Layer Deposition. *Appl. Opt.* **2009**, *48*, 5407−5412.
(53) Zhang, L.; Jiang, H. C.; Liu, C.; Dong, J. W.; Chow, P. Annealing of Al2O3thin Films Prepared by Atomic Layer Deposition. *J. Phys. D: Appl. Phys.* **2007**, *40*, 3707−3713.
(54) Lale, A.; Scheid, E.; Cristiano, F.; Datas, L.; Reig, B.; Launay, J.; Temple-Boyer, P. Study of Aluminium Oxide Thin Films Deposited by Plasma-Enhanced Atomic Layer Deposition from Tri-Methyl-Aluminium and Dioxygen Precursors : Investigation of Interfacial and Structural Properties. *Thin Solid Films* **2018**, *666*, 20−27.
(55) Meyer, D. C.; Levin, A. A.; Paufler, P. Crystalline Coatings of Aluminosilicate Al2SiO5 Polymorphs Formed by Solid State Reaction of Alumina Layers with Silicon/Silica Substrates. *Thin Solid Films* **2005**, *489*, 5−16.
(56) Jakschik, S.; Schroeder, U.; Hecht, T.; Gutsche, M.; Seidl, H.; Bartha, J. W. Crystallization Behavior of Thin ALD-Al_2O_3 Films. **2003**, *425*, 216−220. DOI: 10.1016/s0040-6090(02)01262-2
(57) Lifshits, V. G.; Kaverina, I. G.; Korobtsov, V. V.; Saranin, A. A.; Zotov, A. V. Thermal Annealing Behaviour of Si/SiO2 Structures. *Thin Solid Films* **1986**, *135*, 99−105.
(58) Broas, M.; Kanninen, O.; Vuorinen, V.; Tilli, M.; Paulasto-Kröckel, M. Chemically Stable Atomic-Layer-Deposited Al_2O_3 Films for Processability. *ACS Omega* **2017**, *2*, 3390−3398.
(59) Balakrishnan, G.; Tripura Sundari, S.; Ramaseshan, R.; Thirumurugesan, R.; Mohandas, E.; Sastikumar, D.; Kuppusami, P.; Kim, T. G.; Song, J. I. Effect of Substrate Temperature on Microstructure and Optical Properties of Nanocrystalline Alumina Thin Films. *Ceram. Int.* **2013**, *39*, 9017−9023.
(60) Bull, S. J. Mechanical Response of Atomic Layer Deposition Alumina Coatings on Stiff and Compliant Substrates. *J. Vac. Sci. Technol., A* **2012**, *30*, 01A160.
(61) Cheng, Y.; Qiu, W.; Zhou, K.; Yang, Y.; Jiao, D.; Liu, Z.; Zhong, X. Low-Temperature Deposition of α-Al_2O_3 Film Using Al+α-Al_2O_3 Composite Target by Radio Frequency Magnetron Sputtering. *Mater. Res. Express* **2019**, *6*, 086412.
(62) Herrmann, C. F.; DelRio, F. W.; Miller, D. C.; George, S. M.; Bright, V. M.; Ebel, J. L.; Strawser, R. E.; Cortez, R.; Leedy, K. D. Alternative Dielectric Films for Rf MEMS Capacitive Switches Deposited Using Atomic Layer Deposited Al2O3/ZnO Alloys. *Sens. Actuators, A* **2007**, *135*, 262−272.
(63) Koski, K.; Hölsä, J.; Juliet, P. Deposition of Aluminium Oxide Thin Films by Reactive Magnetron Sputtering. *Surf. Coat. Technol.* **1999**, *116*−*119*, 716−720.
(64) Liu, X.; Haimi, E.; Hannula, S.-P.; Ylivaara, O. M. E.; Puurunen, R. L. On the Reliability of Nanoindentation Hardness of Al_2O_3 Films Grown on Si-Wafer by Atomic Layer Deposition. *J. Vac. Sci. Technol., A* **2014**, *32*, 01A116.
(65) Miller, D. C.; Foster, R. R.; Jen, S. H.; Bertrand, J. A.; Cunningham, S. J.; Morris, A. S.; Lee, Y. C.; George, S. M.; Dunn, M. L. Thermo-Mechanical Properties of Alumina Films Created Using the Atomic Layer Deposition Technique. *Sens. Actuators, A* **2010**, *164*, 58−67.
(66) Ylivaara, O. M. E.; Liu, X.; Kilpi, L.; Lyytinen, J.; Schneider, D.; Laitinen, M.; Julin, J.; Ali, S.; Sintonen, S.; Berdova, M.; et al. Aluminum Oxide from Trimethylaluminum and Water by Atomic Layer Deposition: The Temperature Dependence of Residual Stress, Elastic Modulus, Hardness and Adhesion. *Thin Solid Films* **2014**, *552*, 124−135.
(67) Zywitzki, O.; Hoetzsch, G. Influence of Coating Parameters on the Structure and Properties of Al2O3 Layers Reactively Deposited by Means of Pulsed Magnetron Sputtering. *Surf. Coat. Technol.* **1996**, *86*−*87*, 640−647.
(68) Schütze, A.; Quinto, D. T. Pulsed Plasma-Assisted PVD Sputter-Deposited Alumina Thin Films. *Surf. Coat. Technol.* **2003**, *162*, 174−182.
(69) Islam, A. E.; Nikolaev, P.; Amama, P. B.; Saber, S.; Zakharov, D.; Huffman, D.; Erford, M.; Sargent, G.; Semiatin, S. L.; Stach, E. A.; et al. Engineering the Activity and Lifetime of Heterogeneous Catalysts for Carbon Nanotube Growth via Substrate Ion Beam Bombardment. *Nano Lett.* **2014**, *14*, 4997−5003.
(70) Yang, J.; Esconjauregui, S.; Xie, R.; Sugime, H.; Makaryan, T.; D'Arsié, L.; Gonzalez Arellano, D. L.; Bhardwaj, S.; Cepek, C.; Robertson, J. Effect of Oxygen Plasma Alumina Treatment on Growth of Carbon Nanotube Forests. *J. Phys. Chem. C* **2014**, *118*, 18683−18692.
(71) Zhong, G.; Warner, J. H.; Fouquet, M.; Robertson, A. W.; Chen, B.; Robertson, J. Growth of Ultrahigh Density Single-Walled Carbon Nanotube Forests by Improved Catalyst Design. *ACS Nano* **2012**, *6*, 2893−2903.
(72) Yang, N.; Li, M.; Patscheider, J.; Youn, S. K.; Park, H. G. A Forest of Sub-1.5-Nm-Wide Single-Walled Carbon Nanotubes over an Engineered Alumina Support. *Sci. Rep.* **2017**, *7*, 46725.
(73) van Oss, C. J.; Chaudhury, M. K.; Good, R. J. Interfacial Lifshitz—van Der Waals and Polar Interactions in Macroscopic Systems. *Chem. Rev.* **1988**, *88*, 927−941.
(74) Amama, P. B.; Islam, A. E.; Saber, S. M.; Huffman, D. R.; Maruyama, B. Understanding Properties of Engineered Catalyst Supports Using Contact Angle Measurements and X-Ray Reflectivity. *Nanoscale* **2016**, *8*, 2927−2936.
(75) Amama, P. B.; Putnam, S. A.; Barron, A. R.; Maruyama, B. Wetting Behavior and Activity of Catalyst Supports in Carbon Nanotube Carpet Growth. *Nanoscale* **2013**, *5*, 2642−2646.